Linić, S. Lj., *et al.*: Boundary-Layer Transition Detection by Thermography and ...
THERMAL SCIENCE: Year 2018, Vol. 22, No. 2, pp. 1137-1148

1137

BOUNDARY-LAYER TRANSITION DETECTION BY THERMOGRAPHY AND NUMERICAL METHOD AROUND BIONIC TRAIN MODEL IN WIND TUNNEL TEST

by

Suzana Lj. LINIĆ[a*], Goran J. OCOKOLJIĆ[b], Slavica S. RISTIĆ[c], Vojkan J. LUČANIN[d], Mirko S. KOZIĆ[b], Boško P. RAŠUO[d], and Bore V. JEGDIĆ[e]

[a] Innovation Center of Faculty of Mechanical Engineering, University of Belgrade, Belgrade, Serbia
[b] Military Technical Institute, Belgrade, Serbia
[c] Institute Gosa, Belgrade, Serbia
[d] Faculty of Mechanical Engineering, University of Belgrade, Belgrade, Serbia
[e] Institute of Chemistry, Technology and Metallurgy, University of Belgrade, Belgrade, Serbia

Methods of diagnosing aerodynamic characteristics are constantly developing in order to conduct the precise and energy efficient wind tunnel testing of transport vehicles in the prototype design early stages. This is of a special importance when facing the time/cost consumption problems of detection of the transition zone over the simplified design of the high-speed train. Herein the applied thermodynamics found a very significant role in the field of experimental aerodynamics. With the intention of detecting the boundary-layer transition zone the following measurements were applied: the infrared thermography, flow visualization, and drag force measurements. In addition, the CFD was applied to predict the flow behaviour and transition zone, solving PDE consisting of the Reynolds-averaged Navier-Stokes equations, energy equation, and the equation of state for an ideal gas employing density-based solver. The thermal imaging defined the transition zone by simple application, and fast recognition, while the transition bounds were defined in the analysis. The flow visualization confirmed thermography results and the method itself as favourable, especially in the most expensive early phases of redesigning for aerodynamically optimized and energy efficient solutions. The numerical method was confirmed by the experiments, resulting in acceptable differences in the definition of the transition zone. For a better understanding of the phenomenon, the overlapped implementation of the presented methods focused on forced convection showed as the best solution. Based on the experiences of this research, development of the additional equipment and adjustments will be introduced in the future experiments.

Key words: *aerodynamics, wind tunnel, heat transfer, thermography,
numerical simulation, flow visualization*

Introduction

In the experimental aerodynamics, the most advanced and sensitive test phases are those related to the boundary-layer research. Nowadays, facing the problems of energy

---

* Corresponding author, e-mail: sumonja@yahoo.com

consumption, during wind tunnel (WT) testing, researchers introduced well-known infrared thermography (IRT) into investigating the set of the wind tunnel measuring and visualizing methods. The goal of this work was primarily to investigate the applicability of the thermo-dynamic method – IRT [1], for flow description and boundary-layer transition detection in the experimental practice in the small low-speed WT of the Military Technical Institute (VTI) [2-6] and by the CFD. In addition, the aim was to observe the possibilities of application of the high-speed train testing [4] for defining the requirements for future adjustments, developments of the model, set-up, and the equipment. The expected outcomes were – the reduction of test time, energy consumption, and costs in the early stages of prototype designing.

The multidisciplinary research was performed on the simplified model of the high-speed train (SHST). The SHST was intentionally made simple for the purpose of changes of design parameters, reproduction, easy fabrication and in order to reflect the bio-inspired design [7].

The modern trends in measurements of the boundary-layer and the flow field are focused on non-destructive, energy efficient experimental methods. The high-quality methods are the methods such as the Laser-Doppler anemometry [5], the holographic interferometry [3], the particle image velocimetry (PIV) [8], and IRT. The IRT, for example, is applied in different areas of science and technology, such as fluid dynamics [9, 10], insulation monitoring of the industrial facilities [11, 12], humidity monitoring of buildings, museums and heritage buildings, civil objects energy efficiency detection, the detection of the processes in installations (heating/cooling and electric), inside and out of the rigid walls, studying of the artefacts, inspection of the structure of construction materials, *smart machines*, surveillance and military use, and medicine (IR mammography). In practices, IRT is used for testing in the free flight and in the wind tunnels [1, 13], mostly at high subsonic and supersonic velocities. The CFD is playing a very significant role as the verified and reliable method for flow behaviour prediction around the complex models of vehicles [14], but also for the state-of-the-art large eddy simulations of transient flows or investigation of the boundary-layer and wake behaviour of the bionic designs and surfaces (birds, insects, *etc.*).

Up to now, no universal either experimental or computational method has been found, and it can be said that the best method in research of turbulence phenomenon is actually a set of the overlapping multidisciplinary methods.

Research background

After Prandtl, the boundary-layer was introduced to the flow field description to simplify the calculation methods, thus to *bridge* the Navier-Stokes and the Euler equations [15, 16]. In that sense, the flow over the surface was divided into the outer and inner boundary-layer flow. Herein, Euler and Bernoulli's equations had been applied to the inviscid flow of the outer flow, but later on, the boundary-layer theory was employed related to the viscous flow [17, 18].

The air-flow over the surface of the flat plate (no-slip wall condition) changed its features under the influence of the frictional forces and convection, where the vortices were created only inside the boundary-layer, as shown in fig. 1 [15, 16]. The flow field of the boundary-layer, assuming zero pressure gradient and low turbulence intensity (about 0.1%), evolved from the laminar, transitional to the fully turbulent flow. The laminar flow appeared at the leading edge, firstly stable downstream, and afterwards in a form of Tollmien-Schlichting (T-S) waves. Before the flow becomes fully turbulent it experiences the turbulent spot phase filled with the new turbulent cores, concentrated at the imaginary edge [15, 16].
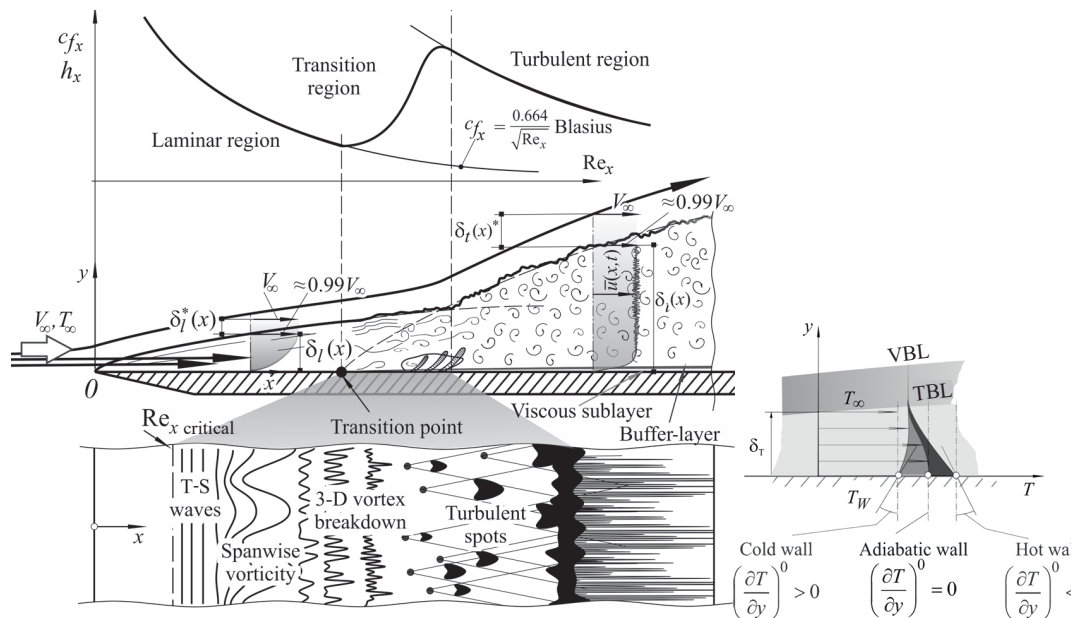
Figure 1. Boundary-layer over the flat plate [15, 16]

As for the smooth flat plate, the transition zone occurs over the length between minimal and maximal values of c_{fx}, which is highly dependent on the turbulence level of the free flow and the local Reynolds number, fig. 1(a). Considering the flow over the hot model, the temperature field is similar to the velocity field and they mutually interact [15-17]. The similarity of behaviours supported the introduction of the term of a thermal boundary-layer (TBL), fig. 1(b). The concept of the TBL introduces the TBL edge, similar to the velosity boundary-layer (VBL), described by 0.99 T_∞. The temperature distribution, across the TBL, depends on the condition of the wall, thus it differs due to the model wall temperature (cold/adiabatic/hot). The heat transfer analysis, in the forced flow over the wall, q, leads to equalization of the heat transfer transmitted from the wall and heat convection. Applying the Fourier and Newton's laws of cooling onto the wall surface, the heat flux is $q = k_{fluid}(\partial T/\partial y) = \overline{h}\,(T_W - T_\infty)$, where the heat transfer coefficient $\overline{h} = 0.5\,c_f V_\infty\,k_{fluid}/\nu$ is dependent on c_f and thermal conductivity of the fluid, k_{fluid} [15-17]. In the case of the hot wall, minimal temperature occurs at the beginning, while the maximal value is achieved at the end of the flow transition. Herein, the IRT camera is measuring rightfully $\Delta T_{IRT} = (T_W - T_\infty)$. In terms of model fabrication for the IRT measurement, the main concerns are subjected to the constancy of the model wall-free flow temperature difference [13]. Mutual dependence of the velocity and temperature is described by the Prandtl number, Pr = $= \mu c_p/k$, thus Pr < 1 leads to $\delta_{TBL} > \delta_{VBL}$ [15-17]. In the practices of the applied aerodynamics and thermodynamics, it is essential to determine the temperature distribution as well as the other flow parameters [2].

In further, recalling the influence of the c_{fx}, one may note that c_{fx} is an essential part in production of the frictional drag force, $D_f = c_f A\rho V^2/2$, and consequently, it influences the consumed power of the future heavy vehicle [15, 16], thus flow laminarization leads to c_D decrease.

The radiation of the real bodies differs from the referent – blackbodies, thus the three types of radiation transfer are defined, with respect to the body of interest: absorptance, α_λ, reflectance, ρ_λ, and transmittance, τ_λ, thus $\alpha_\lambda + \rho_\lambda + \tau_\lambda = 1$, depending on the wavelength, λ [17, 19]. The

real objects, considered as the grey bodies, radiate with respect to their material characteristics – emissivity and the characteristics of IR radiation. Herein the emissivity denotes the spectral emissivity coefficient – the body's ability of radiation emission, $\varepsilon_\lambda = E_\lambda/E_{\lambda\text{black}} \le 1$, and when included into the Stefan-Boltzmann equation, the total emissive power of the grey body is $E^T_{\text{grey}} = \varepsilon_\lambda \sigma T^4$ [17, 19]. The total radiation power, in general, is expressed as a sum of three radiation sources – object, near bodies and atmosphere, in mutual interaction, reduced for the radiation transfer coefficients ($\alpha_\lambda, \rho_\lambda, \tau_\lambda$). The phenomenon of thermal radiation is the basis of the IRT [19].

Experimental set-up

The experimental procedure was divided into the separate measurements of the aerodynamic drag of the SHST model with the ground effect, temperature distribution measurement, and the visualization of the flow of the oil emulsion.

The WT T-32, in question, is the small low-speed WT of the VTI. The WT T-32 is the closed-circuit WT with semi-opened test section [2-4]. The test section has 2 m long elliptic shape (1.8 × 1.2 m). The maximal operational velocity is 60 m/s, ±0.1 m/s, *TF* = 1.14, under atmospheric temperature and pressure [2-4]. The SHST model and the ground model, in form of a flat plate, were fixed independently on clearance of 8 mm, and stationary during tests, as shown in fig. 2.
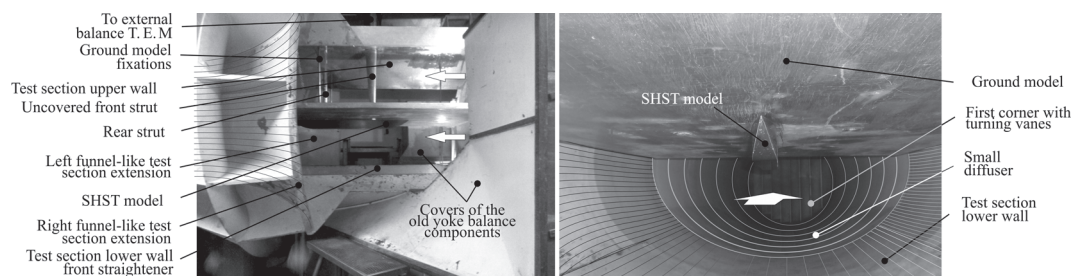

Figure 2. The SHST set-up in the test section of the WT T-32 [2, 4]

The SHST model was designed under the requirements of simplicity, bionics [20], experience [2-4] and recommendations [9, 13], fig. 2. The model has flat sides and sharp edges to emphasize the flow behaviour, tracing the influences of geometry parameters and easy manufacturing. The software PRO/Engineer WF 4 created the SHST numerical model after it was manufactured from 1 m long piece of linden, 60 × 75 mm in cross-section and the nose radius for elongation parameter of $l/h = 3$ (to reflect the bio-inspired design). The nose tip displacement from the ground model leading edge was 0.6 m. The SHST model was painted black and its surface was sandblasted.

The six-component external balance T. E. M. 366 of pyramidal type, in the WT T-32, supported the SHST model and measured its drag force, D_f, in a range of ±550 N, 0.02% front strut (FS), fig. 2 [2].

The emitted radiation from the model depends on surface temperature, where the IRT camera records, calculates, and represents surface temperature data in a form of colourful image – a thermogram. The IRT camera FLIR E40 SC, of industrial class, measured temperatures on the visible surfaces in the range of $T = 253\text{-}393$ K, ±2% (thermal sensitivity <0.07 ºC at 30 ºC), image frequency 30 Hz and IR resolution 320 × 240. The set-up in the wind tunnel for thermal imaging is shown in fig. 3 [19]. The FLIR Researcher software recorded the thermograms, and open source software – Paint Net emphasized the details.

The calculated output signal from the object, considered as the blackbody at T_{obj}, is $U_{obj} = (1/\varepsilon_{obj}\tau_{obj})U^T - [(1-\varepsilon)_{obj}/\varepsilon_{obj})]U_{refl} - [(1-\tau)_{atm}/(\varepsilon_{obj}\tau_{atm})]$, where U^T denotes measured IRT

camera output, U_{refl} and U_{atm} – theoretical output voltages for the blackbody of T_{refl} and T_{atm}, respectively, obtained by the calibration [19]. The accuracy of the IRT measurement depends on the inputs, thermal sensitivity, scanning speed, image resolution, and intensity resolution [1, 13, 19]. In addition, the quality of the thermal imaging depends on conductivity and emissivity of the observed surfaces, and relative position of the influencing reflections from the environment to the IRT camera.
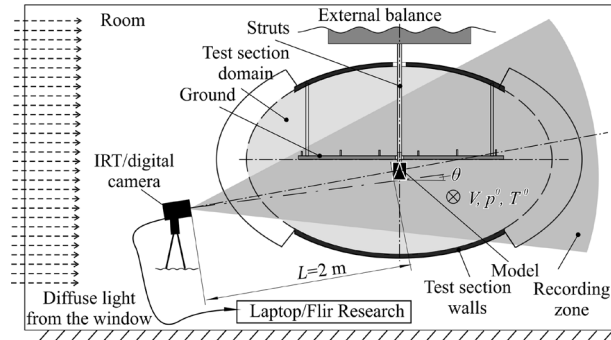

Figure 3. Set-up for thermal imaging, downstream view

The flow visualization was made with the oil emulsion (paraffin oil: 30 ml, olean acid: 5 ml, and 10 g of TiO_2) [3, 4].

Numerical set-up

The numerical study served to predict the flow around the SHST, after adjustments which had the acceptable influence on the results. The applied CFD software was the ANSYS Fluent 12, the control volume based method for calculation of the flow parameters [16, 21, 22].

Compared to the real wind tunnel set-up, the numerical domain resembled the shape of an elliptic cylinder, equal the test section cross-section of the T-32, but prolonged up to 6 m, fig. 4.
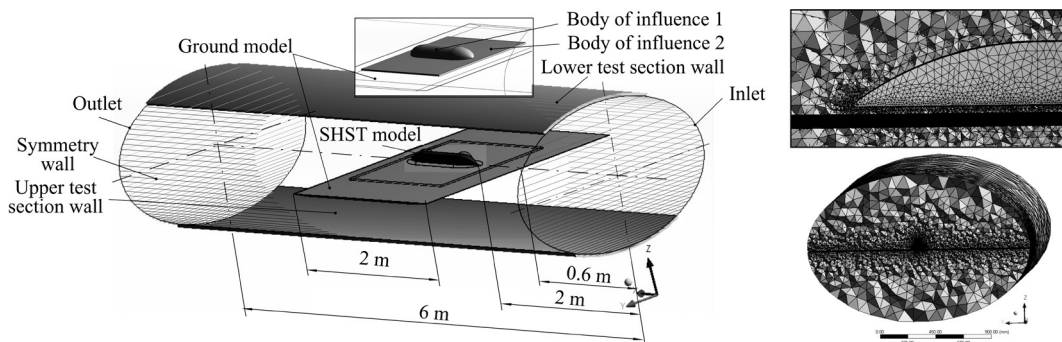

Figure 4. Numerical domain with the SHST and ground models

The mesh of 1.270.607 mixed cells, with the prisms in the inflation layer, was built by introducing the two bodies of influence for better quality, following the criterion of the height of the first layer, $30 < y^+ < 300$ (cell skewness from $0.2 - 0.5$, over $27 - 10\%$ of total cell quantity, respectively). The mesh was selected from the series, performed for the selected numerical set-up: non-adapted (final mesh), the first and second time adapted boundary, adapted to specific y^+ interval, adaption of the forebody region, and third time adapted boundary. In this order of mesh refinements, relative increase of calculation duration per unit iteration was nearly exponential on relative mesh size increase, in relation to the final mesh. The final

mesh answered both criteria, the requirements of y^+ and calculation duration, in contrast to the others ($y^+ = 5 - 30$).

The compressible flow was modelled with the density-based solver, to obtain the temperature distribution over the surfaces [18, 21, 22]. The operational and boundary conditions were defined in accordance with the real test: inlet as pressure-far-field, outlet as pressure outlet, test section walls of aluminum (upper and lower), ground model as a wooden wall, SHST model as a wall of $CaCO_3$ (paint component with similar thermal characteristics), and the others – the symmetry walls, fig. 4.

The turbulence was solved employing mutually the Spalart-Allmaras (S-A) model and energy equation. In general, the S-A model is used for the wall-bounded and boundary-layer flows. It is created to resolve the viscosity-affected regions for meshes providing either $y^+ = 1$ or $y^+ \geq 30$, throughout a single conservation equation with built damping functions [18, 21, 22]. The S-A model was selected for its simplicity and time/cost efficiency for large mashes, compared to the others. The solving method involved the implicit scheme, the Roe flux-difference splitting scheme flux type, and the Green-Gauss node based method of discretization as well as the second order functions. The use of full multi-grid (FMG) initialization, for the subsonic flow, was aimed at better determination of the beginning solution, and faster convergence.

Results and discussion

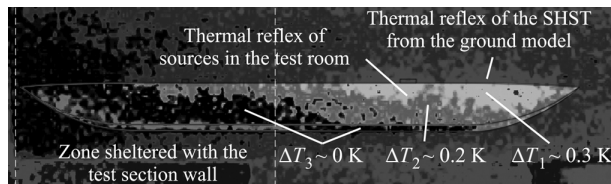The thermogram in fig. 5, showing the temperature non-uniformity at the equilibrium state, originated from the thermal reflexes (from the SHST and other bodies) and holding the three significant zones used for result corrections. Figure 6 shows the uncorrected thermogram of the wind-on phase scene, at $V = 50$ m/s, $T = 296$ K.

Figure 5. Temperature distribution over the SHST in the equilibrium state

In case of the partial coating of SHST with the emulsion, the flow spread the coating from the nose to the tail, leaving the imprint of five flow regions, as shown in fig. 7.
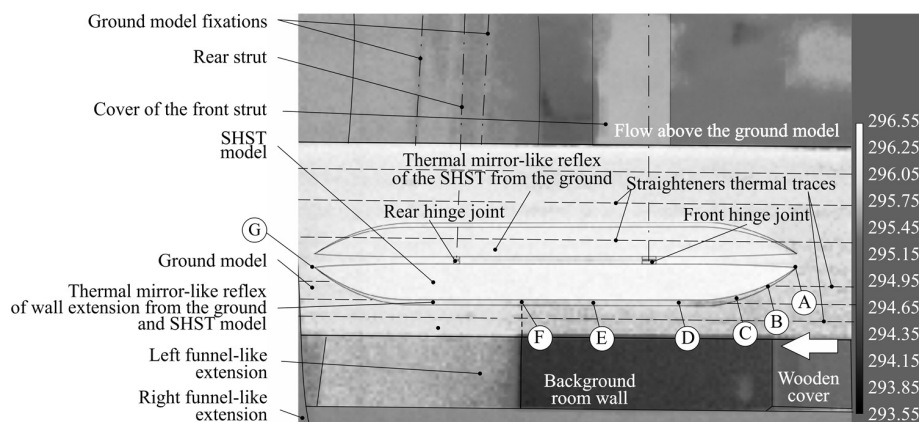

Figure 6. Thermal image of the test scene ($V = 50$ m/s, $T = 293.15$ K)
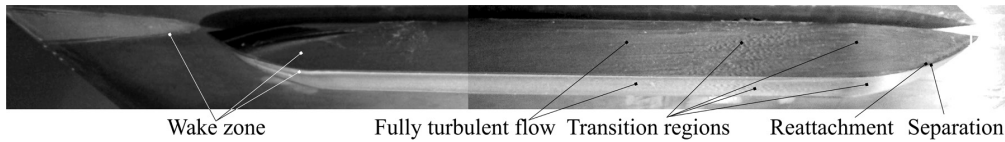
Linić, S. Lj., *et al.*: Boundary-Layer Transition Detection by Thermography and ...
THERMAL SCIENCE: Year 2018, Vol. 22, No. 2, pp. 1137-1148

1143

Wake zone   Fully turbulent flow   Transition regions   Reattachment   Separation

Figure 7. Flow visualization after partial covering with the oil emulsion (V = 50 m/s)

The experimentally visualized traces and the numerically obtained pathlines, coloured by temperature, are shown in fig. 8. The main difference was indicated in the central side view, where the oil traces showed slightly more inclined paths. Therefore, for achieving the more realistic results, the investigations in the field of $y^+ = 1$ are necessary, together with the application of the enhanced wall treatment or the SST based transition model, with the support of the advanced IT resources.
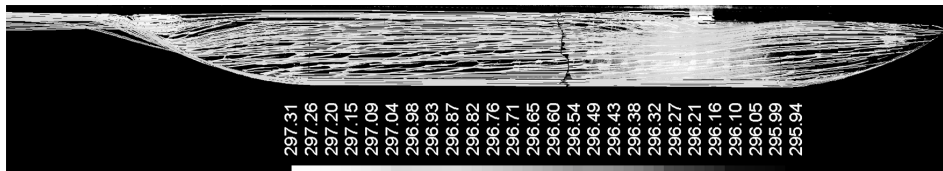

Figure 8. Flow pattern and flow pathlines, coloured by temperature,
(V = 50 m/s, Re $\approx$ 237000)

Figure 9 shows the local values of T, c_f, p, M, and Pr along the centre line, estimated by the CFD. The transition region along the centre line began at x = 0.17 m – 0.19 m from the nose tip. The end of the transition region was at $x \approx$ 0.41 m. In the present case, $\delta_{V\,\text{turb.}} \approx$ 2-3 mm, $\delta_{T\,\text{turb.}} \approx$ 5 mm. Good correlation with flow imprint, fig. 7, verified the CFD method.
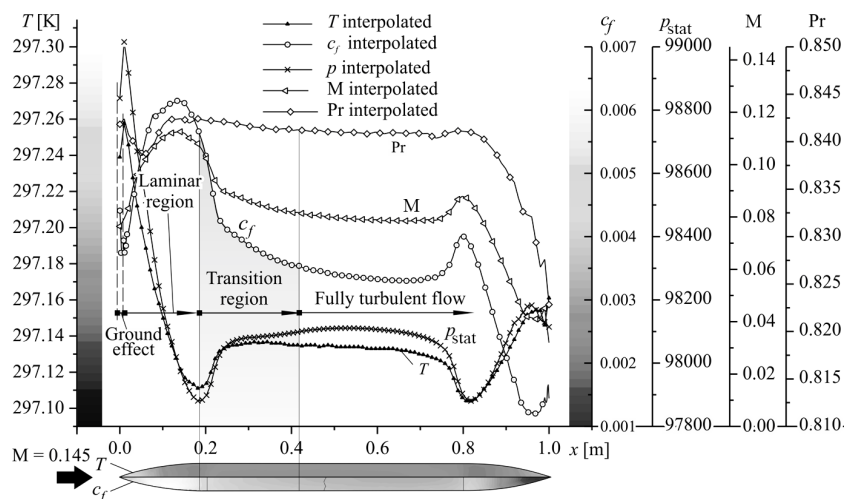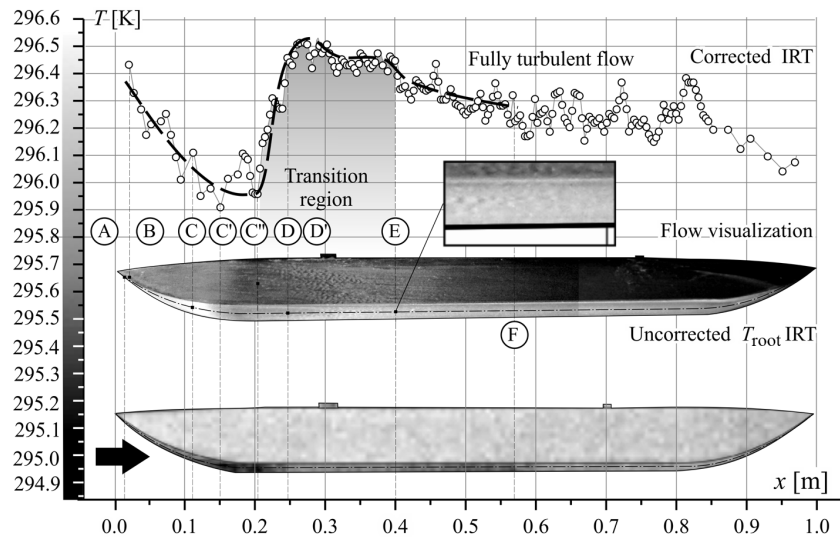

Figure 9. Selected flow parameters over the SHST roof, along the centre line,
**obtained with CFD (V = 50 m/s, Re $\approx$ 237000)**

The local temperature values on the roof, along the centre line, and the temperature distribution estimated by IRT are shown in fig. 10. The finish of transition arose at the end of

Figure 10. Temperature distribution over the SHST surfaces obtained by the IRT measurements

wavy oil traces, which corresponds, to the flow parameters near the spot "E". The $T_{C'}$ was interpreted as an influence of the scratch on the leading edge, and it was out of interest.

The maximal temperatures, measured along the lines in fig. 11, marked in "E1-E7", were interpreted as the ending points of the transition region from the side. The flow imprints in figs. 10 and 11 are in good correlation with the IRT readings along seven measuring lines and verified the method.
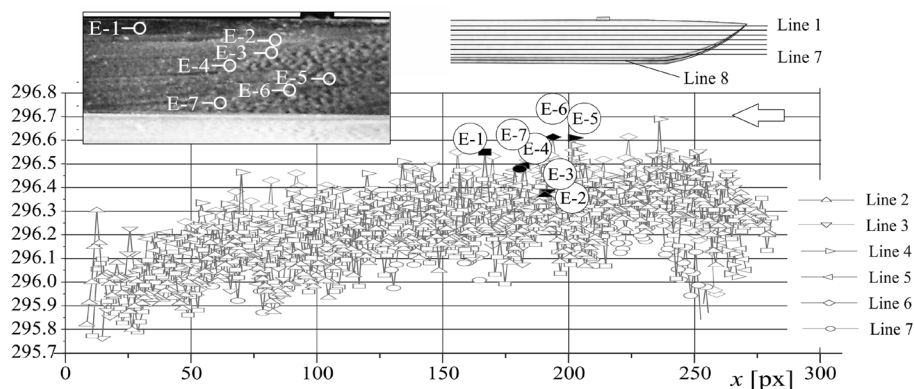

Figure 11. Determination of the ends of the transition region along seven measuring lines from the side of the SHST (corrected values)

The detailed study was made in prior to the zone of the SHST nose, in which the transition started, as shown in fig. 12.

Flow visualization, from fig. 12(a), confirmed the IRT data, fig. 10, and CFD, fig. 9. Herein, the washed-out line, from the nose roof across the leading edge, was interpreted as the reattachment that occurred after the laminar separation. Besides, the traces of the T-S waves were following the leading edge and interacted with the separated and reattached flow, which
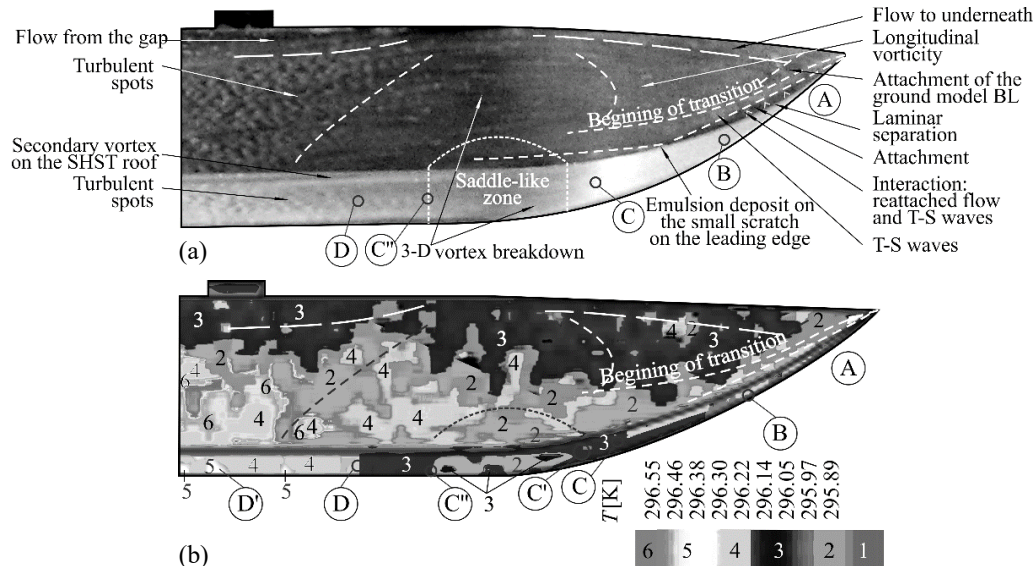
Figure 12. Flow patterns over the SHST nose; (a) flow imprint in the partially applied oil emulsion and (b) manually corrected static temperature distribution from the IRT

was represented in the cyclic local widening of the line of reattachment. Downstream, there were three different areas of the transition zone, fig. 12(a), downstream from a dashed line: the longitudinal vorticity zone, the 3-D breakdown zone in which the turbulent spots were formed, and the zone of turbulent spots, which formed water-like waves in deposits of TiO_2. Over the SHST roof, the first presence of the water-like waves was recognized just downstream from the "C'". Therefore, the surface with higher curve gradients and thickness of the profile, the same as on the SHST roof, resulted in the narrowing of the transition zone. From fig. 12(a) it is clear that the flow collided with the hinge joint, entered into the mainstream and twisted it. The influence may be avoided by adaptations such as introducing the model sting support.

The corrected IRT data, in fig. 12(b), represented the laminar and transition regions, flow affected by the ground and the flow induced by the gap and joints. The five coloured zones differ over the side surfaces ($T_2 - T_6$). The portion of the flow from the ground boundary-layer was affecting the flow around the nose tip (T_3). The laminar flow was hardly detected over the roof due to low resolution, but in the approximation, it was marked between "A – C", starting outside of the ground TBL. The zones of T_2 and T_4, from the side and just after the leading edge, were the zones of the unstable laminar flow with the laminar separation and reattachment and they were indicated by comparison with the flow visualization. The small damage at the nose leading edge caused forming of the emulsion deposit, leaving a short wake downstream. The early temperature drop and the signs of the wake were also indicated in the thermogram, both on the side and the roof, leaving a false expression of the T_{min} due to 2-D representation and low resolution. The real indication of the transition beginning was noticed along the saddle-like edge length, starting from "C'", over the local roof width. The CFD indicated the saddle-like zone, covering the 3-D vortex breakdown zone ($T_{min} = T_2$), and the arced surface on the side. Due to different geometry parameters ($l/h = 3$ for the roof and $l/h = 7.5$ on the side), the arced zone on the side did not represent the transition beginning. Just downstream from the saddle-like zone on the roof, the zone with the turbulent spots was formed throughout the middle. This zone, surrounded by the secondary vortex flow, originated from the flow over the sharp

1146

Linić, S. Lj., *et al.*: Boundary-Layer Transition Detection by Thermography and ...
THERMAL SCIENCE: Year 2018, Vol. 22, No. 2, pp. 1137-1148

edges of the SHST. The zones containing the turbulent spots were indicated in the areas with the locally highest temperatures. The zone of turbulent spots was blown out by the flow from the gap on the side.

In this paper, the investigations made by IRT and CFD showed the applicability of methods in conditions without the flow separation, where the transition zone was defined by the data analysis of the overlapped results. The main difficulties in defining the transition zone were set-up adaptation and the data corrections. IT resource development would contribute CFD boundary-layer tests, too.

The CFD results were also verified through drag coefficient – calculated $c_{D\,\text{CFD}} = 0.3$ with WT result $c_{D\,\text{WT}} = 0.291$, showing good data correlation, $c_{D\,\text{CFD}} \approx 1.03\, c_{D\,\text{WT}}$.

Conclusion

The presented research confirms the thermography as the desirable tool for surface temperature measurements and flow transition detection. It is complementary with the flow visualization, over the complex model geometry, and it offers high reliability, in early stages of prototyping. Flow visualization verified both IRT and CFD through a good correlation of the results in the determination of the transition zone and the flow over the model surfaces. Possibilities of application of the IRT in the wind tunnel testing are confirmed although the IR camera was of the industrial class. The IRT is a valuable method for time-cost-saving, for the most delicate research of boundary-layer transition detection. In fact, IRT, flow visualization, and CFD represent a set of methods, with an excellent ability for detection and prediction of key zones in the flow, in the early stage of the designing and concept selection process, as well as the foundation for further advanced boundary-layer investigations. The non-destructive methods proved to be reliable, affordable, and fast, requiring the minimal adaptations of the model set-up, easy for use in various positions and environmental conditions. However, this research highlighted the necessity of more precise, qualitative and quantitative analysis of the flow transiency that might be improved by implementation of the high-speed and high-resolution IRT camera, while the advanced IR resources might describe the boundary-layer flow more realistically using the CFD. Future tests will include adaptations of the test set-up – model and environment, to contribute the IRT precision. Furthermore, the introduction of additional measuring and visualizing methods, such as the smoke visualization (with a stroboscope) and PIV might significantly contribute to the analysis of the complex flow field around the SHST.

Acknowledgment

Nomenclature

A	– surface area, [m²]	D_f	– drag force, [N]
c_D	– drag force coefficient, [–]	E	– energy, [J]
c_f	– skin friction coefficient, [–]	h	– heat transfer coefficient, [Wm⁻²K⁻¹]
c_p	– specific heat at constant pressure, [Jkg⁻¹K⁻¹]	h_x	– height, [m]

Linić, S. Lj., *et al.*: Boundary-Layer Transition Detection by Thermography and ...
THERMAL SCIENCE: Year 2018, Vol. 22, No. 2, pp. 1137-1148

1147

k	– thermal conductivity, [Wm^{-1}K^{-1}]		ρ_λ	– reflectance, [–]
L	– length, [m]		ρ	– density [kgm^{-3}]
M	– Mach number (= V/c), [–]		σ	– Stefan-Boltzmann constant, [Wm^{-2}K^{-4}]
Pr	– Prandtl number (= $\mu c_p/k = \nu/\alpha$), [–]		τ_λ	– transmittance, [–]
p	– pressure, [Pa]			
q	– heat flux, [Wm^2]		*Subscripts*	
Re	– Reynolds number (= $V l/\nu$), [–]		∞	– free stream condition,
T	– temperature, [K]		atm	– atmosphere,
TF	– turbulence factor, [–]		f	– product of friction,
U	– output, [V]		obj	– object
V	– velocity, [m/s]		refl	– reflected,
x	– spatial co-ordinate, [m]		turb	– turbulent,
y	– spatial co-ordinate, [m]		W	– wall condition,
y^+	– dimensionless distance from the surface of the first mesh layer, [–]			

Greek symbols

Acronyms

α	– thermal diffusivity (=$k/\rho c_p$), [m^{2}s^{-1}]	BL	– boundary-layer,
α_λ	– absorptance, [–]	CL	– centre line,
ε_λ	– emissivity, [–]	IRD	– infrared thermography
δ	– boundary-layer thickness, [m]	PIV	– particle image velocimetry,
λ	– wavelength, [m]	S-A	– Spalart-Allmaras turbulent model,
μ	– viscosity, [kgm^{-1}s^{-1}]	SHST	– simplified model of the high-speed train,
ν	– kinematic viscosity, [m^{2}s^{-1}]	TBL	– thermal boundary-layer,
		VBL	– velosity boundary-layer
		WT	– wind tunnel

References

[1] Astarita, T., Carlomagno, G. M., *Infrared Thermography for Thermo-Fluid-Dynamics*, Springer-Verlag, Berlin Heidelberg, Germany, 2012
[2] Linić, S., Mrkalj, N., *Wind Tunnel Design and Testing*, Institut Goša, Belgrade, 2017
[3] Ristić, S., *et al.*, Turbulence Investigation in the VTI's Experimental Aerodynamics Laboratory, *Thermal Science, 20* (2016), Suppl. 6, pp. S1-S14
[4] Ristić, S., *et al.*, High Speed Train Model Testing in T-32 Wind Tunnel by Infrared Thermography and Standard Methods, *Proceedings*, 7th International Scientific Conference on Defensive Technologies, OTEH 2016, The Military Technical Institute, Belgrade, 2016, pp. 35-40
[5] Ristić, S., *et al.*, Estimation of Laser-Doppler Anemometry Measuring Volume Displacement in Cylindrical Pipe Flow, *Thermal Science, 16* (2012), 4, pp. 1027-1042
[6] Ristić, S., Flow Visualisation Techniques in Wind Tunnels Part I – Non optical Methods, *Scientific Technical Review*, *57* (2007), 1, pp. 39-50
[7] Linić, S., *et al.*, Comparison of Numerically Obtained 2D Flow Fields for the Bionic High Speed Train Concept Designs Inspired with Aquatic and Flying Animals, *Proceedings,,* 6th International Scientific Conference on Defensive Technologies, OTEH 2014, The Military Technical Institute, Belgrade, Serbia, 2014, pp. 44-49
[8] Čantrak, Dj. S., *et al.*, Time-Resolved Stereo PIV Investigation of the NASA Common Research Model in the NASA Ames Fluid Mechanics Laboratory 32- by 48-in Indraft Wind Tunnel, Center for Turbulence Research Annual Research Briefs, 2014, pp. 179-191
[9] Laurinavicius, D., *et al.*, Measurement of Water Temperature and Velocity Fields by Applying Thermography on Two-Phase Flow through Horizontal Rectangular Channels, *Thermal Science*, On-line first, https://doi.org/10.2298/TSCI160502129L
[10] Montelpare, S., Ricci, R., A Thermographic Method to Evaluate the Local Boundary Layer Separation Phenomena on Aerodynamic Bodies Operating at Low Reynolds Number, *International Journal of Thermal Sciences, 43* (2004), 3, pp. 315-329
[11] Kozić, M., *et al.*, Determination of the Temperature Distribution on the Walls of Ventilation Mill by Numerical Simulation of Multiphase Flow and Thermography, *Proceedings*, 5th International Congress of Serbian Society of Mechanics, Arandjelovac, Serbia, 2015
[12] Andjelković, B. R., *et al.*, Modeling Steady-State Thermal Defectoscopy of Steel Solids Using Two Side Testing, *Thermal Science*, *20* (2016), Suppl. 5, pp. S1333-S1343

1148

Linić, S. Lj., *et al.*: Boundary-Layer Transition Detection by Thermography and ...
THERMAL SCIENCE: Year 2018, Vol. 22, No. 2, pp. 1137-1148

[13] Simon, B., *et al.*, IR-Thermography for Dynamic Detection of Laminar-Turbulent Transition, *Proceedings*, 18th International Symposium on the Application of Laser and Imaging Techniques to Fluid Mechanics, Lisbon, Portugal, 2016

[14] Ahmed, S., R., Numerical Methods for Computation of Flow around Road Vehicles, in: *Aerodynamics of Road Vehicles: from Fluid Mechanics to Vehicle Engineering* (Ed. W.-H. Hucho), Butterworth-Heinemann, London, 1990, pp. 480-537

[15] White, F. M., *Viscous Fluid Flow*, 2nd ed., McGraw-Hill, New York, USA, 1991

[16] Schlichting, H., *Boundary-Layer Theory*, 7th ed., McGraw-Hill, New York, USA, 1979

[17] Lienhard IV, J. H., Lienhard V, J. H., *A Heat Transfer Textbook*, Phlogiston Press, Cambridge Mass., USA, 2008

[18] Versteeg, H. K., Malalasekera, W., *An Introduction to Computational Fluid Dynamics – The Finite Volume Method*, LONGMAN, Harlow, England, 1995

[19] ***, User's Manual, FLIR Exxx series, FLIR Systems, Pub.No. 7559597, December, 2010

[20] Rašuo, B., *Bionika u dizajnu* (*Bionics in Design* – in Serbian), Faculty of Mechanical Engineering, University of Belgrade, Belgrade, eBook on CD, 2014

[21] ***, ANSYS Fluent 12 User's and Theory Guide, ANSYS Inc., 2009

[22] Kozić, M., *Primena Numeričke Dinamike Fluida u Aeronautici* (*Application of the Computation Fluid Dynamics in Aeronautics* – in Serbian), Naučnotehničke informacije, The Military Technical Institute, Belgrade, 2013